

# Second-order topological insulator in periodically driven lattice

Ying Lei,<sup>1</sup> Xi-Wang Luo,<sup>2</sup> and Shaoliang Zhang<sup>1,3,\*</sup>

<sup>1</sup>*School of Physics, Huazhong University of Science and Technology, Wuhan 430074, China*

<sup>2</sup>*Key Laboratory of Quantum Information, University of Science and Technology of China, Hefei, Anhui 230026, China*

<sup>3</sup>*State Key Laboratory of Quantum Optics and Quantum Optics Devices, Shanxi University, Taiyuan 030006, China*

(Dated: February 21, 2022)

The higher-order topological insulator (HOTI) is a new type of topological system which has special bulk-edge correspondence compared with conventional topological insulators. In this work, we propose a scheme to realize Floquet HOTI in ultracold atom systems. With the combination of periodically spin-dependent driving of the superlattices and a next-next-nearest-neighbor  $d$ -wave-like anisotropic coupling term between different spin components, a Floquet second-order topological insulator with four zero-energy corner states emerges, whose Wannier bands are gapless and exhibit interesting bulk topology. Furthermore, the anisotropic coupling with nearest-neighbor form will also induce some intriguing topological phenomena, e.g. non-topologically protected corner states and topological semimetal for two different types of lattice structures respectively. Our scheme may give insight into the construction of different types of higher-order topological insulators in synthetic systems. It also provides an experimentally feasible platform to research the relations between different types of topological states and may have a wide range of applications in future.

## I. INTRODUCTION

In the last few years, higher-order topological insulator, as a new type of topological matters with unconventional bulk-edge correspondence, has attracted intensive interests [1–16] in communities of topological physics and condensed matter physics. For example,  $n$ -dimensional second-order topological insulator (SOTI) has topological protected gapless  $(n-2)$ -dimensional edge states while the  $(n-1)$ -dimensional boundaries are gapped, which is very different from conventional topological matters with topological protected gapless  $(n-1)$ -dimensional boundaries. People have proposed considerable interesting models to construct HOTI. One of the most prominent proposals is the extension of one-dimensional (1D) Su-Schrieffer-Heeger (SSH) model [17] to the two-dimensional (2D) system [1, 2]. With an additional  $\pi$  flux threaded through each plaquette, the SOTI can be constructed and the topological properties are characterized by the quantized quadrupole moment and edge polarization in the system. Another important proposal is based on a 2D topological insulator (TI) such as Berner-Hughes-Zhang (BHZ) model with an additional  $d$ -wave-like anisotropic coupling term [18]. In this models, the emergence of topologically protected zero-energy corner states can be explained by the low-energy effective theory. In addition, the concept of HOTI is extended into many-body systems, and higher-order topological superconductors are proposed [19–23], which support Majorana zero modes [24–26] that can be potentially applied to topological quantum computation.

Recently, the research about HOTI is developing very rapidly. A lot of schemes to construct HOTI is put forward in different types of materials in condensed matter physics, and relevant experimental phenomena have been observed, e.g., in bismuth [27]. On the other hand, zero-energy corner states have also been realized experimentally [28–30] in many syn-

thetic systems such as photonic crystals, electronic circuits and microwave resonators. Remarkably, ultracold atom system is proposed to be an ideal synthetic platform to simulate many fascinating topological phenomena. Due to its highly controllable properties, not only those theoretically proposed topological models can be realized in experiments, but also some new types of topological matters and other intriguing quantum phenomena might be predicted and explored in ultracold atom system. In particular, direct measurements of bulk topology are accessible for most experiments using ultracold atom [31, 32], as compared with other synthetic systems.

In this work, we propose an experimentally feasible model of SOTI based on ultracold atoms in optical lattices. We confine ultracold atoms which have two hyperfine spin states in a checkerboard lattice. By applying a spin-dependent circular driving [33, 34], the whole system can be regarded as an effective 2D TI [35–37] with gapless edge states which are protected by  $Z_2$  symmetry. Then by adding an additional next-next-nearest-neighbor (NNNN) anisotropic coupling between different spin components, the edge states will be gapped out and topologically protected zero-energy corner states arise at the intersection of adjacent boundaries. Different from earlier works, the Wannier bands for characterizing the bulk topology are gapless. However, the topological invariant in the bulk can still be well-defined due to the reflection symmetries in our discussion. In this work, the coupling between different spin components has a  $d$ -wave form instead of the chiral  $d + id$  one, thus the next-nearest-neighbor (NNN) coupling is irrelevant and don't need to be considered. Furthermore, when the NNNN anisotropic coupling term is replaced by the conventional nearest-neighbor (NN) anisotropic coupling, one can also find that there exist interesting topological phenomena, such as non-topologically protected corner states and topological semimetal [38–40] for different NN coupling terms respectively. This work provides a new perspective to understand the relationship between the choice of anisotropic coupling term and the emergence of higher-order topological insulator. In addition, the proposed model enriches theoretical research about HOTI and may have a wide range of applica-

\* shaoliang@hust.edu.cn

tions in future.

This paper is organized as follows. In Section II, we introduce our model and its topological properties. We also give an explanation about the emergence of zero-energy corner states with an effective edge theory and the bulk-edge-corner correspondence. In Section III, topological phenomena induced by the two types of NN coupling term are discussed, i.e. non-topologically protected corner states and topological semimetal with one or two pairs of nodal points. In Section IV, we extend our model into a three-dimensional system and discuss its topological properties. In such a system, chiral hinge modes and the swing of corner states can be observed. Section V is devoted to the proposal of experimental setup and measurements. Section VI is a conclusion.

## II. THE MODEL AND TOPOLOGICAL PROPERTIES

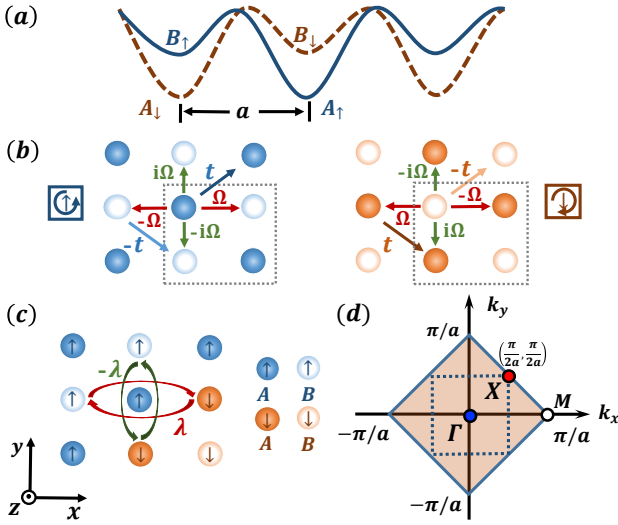


FIG. 1. Scheme of 2D TI model with open boundary along the ABA direction. (a) The lattice potentials for different spin components along the  $x$  direction, where  $A$  and  $B$  represent sublattices with an energy detuning. Blue solid lines and orange dotted lines are associated with lattice structures for spin-up and spin-down components respectively. (b) The lattice structure. Shaking directions are spin-dependent, i.e. the directions for spin-up and spin down are anti-clockwise and clockwise respectively. Dark and light colors represent  $A$  and  $B$  sublattices respectively. The nearest-neighbor tunnelings have opposite chirality because of the spin-dependent shaking. (c) Anisotropic coupling term. NNNN coupling between different spin components along the  $x$  and  $y$  directions are  $\lambda$  and  $-\lambda$  respectively. (d) The colored area is the Brillouin zone (BZ) of the 2D TI model. The square surrounded by the dash line is the folded BZ.

The model we discuss in this work is based on a spin-dependent two-dimensional checkerboard lattice, the spin-up and spin-down components of which are shifted from each other by length  $a$  along the  $x$  or  $y$  direction, where  $a$  is the displacement from site  $A$  to its nearest-neighbor (NN) site  $B$ , as depicted in Fig.1(a) and (b). Due to the energy detuning between the sublattices  $A$  and  $B$ , the tunnelings be-

tween nearest-neighbor (NN) sites are forbidden. Then by applying a synthetic gauge fields [41] with opposite directions of circular shaking for different spin components, one can induce an unconventional NN tunneling with opposite chirality for different spin components and an effective next-nearest-neighbor (NNN) tunneling with opposite signs for  $A$  and  $B$  sublattices respectively, as shown in Fig.1. Additionally, by adding an NNNN anisotropic coupling between different spin components, see in Fig.1(c), the zero-energy corner states appear, which signifies the emergence of SOTI. According to the Floquet theory in Ref. [41], the tight-binding Hamiltonian of our system in the momentum space can be described as  $H = \sum_{\mathbf{k}} \Psi_{\mathbf{k}}^{\dagger} H_{\mathbf{k}} \Psi_{\mathbf{k}}$  with  $\Psi_{\mathbf{k}}^{\dagger} = [a_{\mathbf{k},\uparrow}^{\dagger}, b_{\mathbf{k},\uparrow}^{\dagger}, a_{\mathbf{k},\downarrow}^{\dagger}, b_{\mathbf{k},\downarrow}^{\dagger}]^{\text{T}}$  and

$$H_{\mathbf{k}} = \{\delta + 4t \cos(k_x a) \cos(k_y a)\} \sigma_z + 2\Omega \sin(k_x a) \sigma_y + 2\Omega \sin(k_y a) \sigma_x s_z + 2\lambda \{\cos(2k_x a) - \cos(2k_y a)\} \sigma_x s_x \quad (1)$$

where  $s_i, \sigma_i$  ( $i = x, y, z$ ) denote the Pauli matrices acting on the hyperfine spin ( $\uparrow, \downarrow$ ) and orbit ( $A, B$ ) degree of freedoms respectively,  $2\delta$  is the effective energy detuning between sublattices  $A$  and  $B$ ,  $\Omega$  and  $t$  are the amplitude of NN and NNN tunneling respectively, and  $\lambda$  is the amplitude of the NNNN coupling. In this work, we set  $t > 0$  for convention.

At  $\lambda = 0$ , the Hamiltonian in Eq.(1) and its topological properties are very similar to the BHZ model. We remark that in contrast to the system with a magnetic field breaking the time-reversal symmetry, there exists quantum spin Hall effect (QSHE) in the parameter space of  $|\delta| < 4t$ , i.e. a topological insulator with two opposite quantum Hall phases, the Chern numbers of which satisfy  $C_{\uparrow} = -C_{\downarrow}$ . According to the band structure with open boundary along the  $x$  (or  $y$ ) direction as shown in Fig.2(c), there exists two pairs of edge states that propagate with opposite directions. The Hamiltonian (1) preserves time reversal symmetry and inversion symmetry with corresponding symmetry operators  $\mathcal{T} = i s_y \mathcal{K}$  ( $\mathcal{K}$  denoting the operation of complex conjugate) and  $\mathcal{I} = \sigma_z$  respectively. So we have  $\mathcal{T} H_{\mathbf{k}} \mathcal{T}^{-1} = H_{-\mathbf{k}}$ ,  $\mathcal{I} H_{\mathbf{k}} \mathcal{I}^{-1} = H_{-\mathbf{k}}$ .

For  $\lambda \neq 0$ , the anisotropic coupling term breaks both the inversion symmetry and time-reversal symmetry but respect their combination  $\mathcal{I}\mathcal{T}$ , that is  $(\mathcal{I}\mathcal{T}) H_{\mathbf{k}} (\mathcal{I}\mathcal{T})^{-1} = H_{\mathbf{k}}$ . One can easily verify that  $(\mathcal{I}\mathcal{T})^2 |\psi\rangle = -|\psi\rangle$  is satisfied for arbitrary states  $|\psi\rangle$ , which means that the system has a general Kramers degeneracy and energy bands in whole Brillouin zone (BZ) have a two-fold degeneracy. By exact numerical calculation with open boundary conditions along the  $x$  and  $y$  direction, we find that four zero-energy states emerge and are located at the corners of 2D lattice, see Fig.2(a). The four zero-energy corner states are topologically protected when  $|\delta| < 4t$ , as shown in Fig.2(b). The anisotropic coupling term gap out the energy bands on edge, as shown in Fig.2(d).

The emergence of zero-energy corner states can be revealed from the low-energy effective theory [18]. In this system, the first BZ is a square. At the topological phase boundary, the band gap closes at  $\Gamma = (0, 0)$  and  $M = (\pi/a, 0)$  when  $\delta = -4t$  and  $\delta = 4t$  respectively, as shown in Fig.1(c). When  $\delta \rightarrow -4t$ , the minimum of the gap in the whole BZ is located at  $\Gamma$  point. Then the Hamiltonian (1) can be expanded around

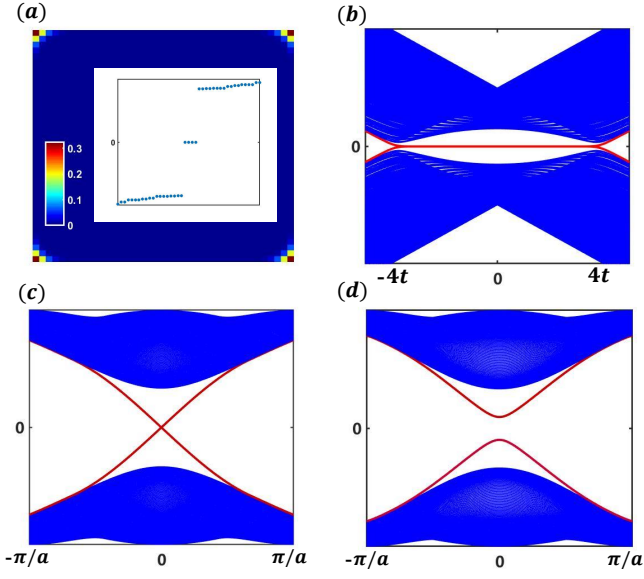


FIG. 2. (a) Probability density distributions of zero-energy corner states with a lattice size  $L_x \times L_y = 40 \times 40$ . The inset shows energy spectrum of the whole system. The parameter of this panel is set as  $\delta = t$ ,  $\Omega = t$  and  $\lambda = t$ . (b) Energy spectrum with values of effective detuning  $\delta$ . (c) Energy-band structure of the system with an open boundary along the  $x$  direction when  $\lambda = 0$ . (d) Energy-band structure of the system with an open boundary along the  $x$  direction when  $\lambda \neq 0$ . The red curves denote two degenerate edge states.

$\Gamma$  point with the low-energy form as

$$H_{\Gamma}(\mathbf{k}) = \{m - 2t(k_x^2 a^2 + k_y^2 a^2)\} \sigma_z + 2\Omega k_x a \sigma_y + 2\Omega k_y a \sigma_x s_z + 8\lambda(k_y^2 a^2 - k_x^2 a^2) \sigma_x s_x \quad (2)$$

where  $m = \delta + 4t$ . We choose the open boundary condition  $y > 0$ , under which  $k_y$  is replaced by  $-i\partial_y$ , and ignore the higher order terms of  $k_x$ , the effective Hamiltonian can be rewritten as  $H_{\Gamma}(k_x, -i\partial_y) = H_0 + H_p$  with

$$H_0 = \{m + 2ta^2 \partial_y^2\} \sigma_z - 2i\Omega a \partial_y \sigma_x s_z \quad (3)$$

and a perturbation term

$$H_p = 2\Omega a k_x \sigma_y - 4\lambda a^2 \partial_y^2 \sigma_x s_x \quad (4)$$

Further,  $H_0$  can be block diagonalized and the two zero-energy solutions are given by

$$\psi_{\uparrow} \propto A(y) \begin{pmatrix} 1 \\ 0 \\ i \\ 0 \end{pmatrix}, \psi_{\downarrow} \propto A(y) \begin{pmatrix} 0 \\ 1 \\ 0 \\ -i \end{pmatrix} \quad (5)$$

where  $A(y) = e^{-C_+ y} - e^{-C_- y}$  and  $C_{\pm} = \frac{\Omega}{2ta} \pm \frac{\Omega}{2ta} \sqrt{1 - \frac{2mt}{\Omega^2}}$ . So when  $\delta > -4t$ ,  $m > 0$ , both  $C_+$  and  $C_-$  are positive, which means that the zero-energy modes are localized on the edge. When  $\delta < -4t$ , we have  $m < 0$  and  $C_- < 0$ , the solution is divergent, implying that there

is no zero-energy edge modes and the system is topologically trivial. Then, we project  $H_p$  into the subspace of these zero-energy edge modes with the form

$$H_{y+}(k_x) \propto D_{y+} k_x s_z - M_{y+} s_y \quad (6)$$

where  $D_{y+} = 4\Omega a \int_0^{\infty} A^2(y) dy$  and  $M_{y+} = 8\lambda a^2 \int_0^{\infty} A(y) \partial_y^2 A(y) dy$ . In the effective edge Hamiltonian (6), the last term  $M_{y+}$  can be viewed as an effective mass. One can use the same method to expand the effective Hamiltonian (2) on the other three edges as demonstrated in Ref. [18] and obtain three other edge Hamiltonians of a similar form. The effective masses on adjacent edges always have opposite signs, which means that the zero-energy "domain wall" emerges on the junction of adjacent edges according to the Jackiw-Rebbi theory [42] when the boundary of system is a square cross section.

In conventional topological systems, the bulk-edge correspondence is important for verifying their topological properties. The emergence of gapless edge states always corresponds to a nontrivial bulk topology. For HOTI, bulk-edge-corner correspondence also exists, i.e. the emergence of zero-energy corner states are associated with edge polarization and non-zero quantized quadrupole moment in the bulk [1, 2]. But in our system, because the open boundary that we choose is along the diagonal lines of the BZ, the choice of the above BZ may not be suitable to explore the topological properties in the bulk. This can also be seen by noticing the zero-energy edge mode solution Eq.5, which is located at the edge of  $y = 0$ , and thus the lattice period in this subspace is  $2a$  along the  $x$  direction, reducing the Bloch momentum  $k_x$  within the dashed square in Fig.1(d). To overcome this difficulty, we can enlarge the size of unit cell to contain four nearest-neighbor sites, as shown in Fig.1(b). Then the BZ will be folded into the range enclosed by the dash line in Fig. 1(d) and the corresponding Hamiltonian in the momentum space can be rewritten as

$$H_{\mathbf{k}} = H_{\mathbf{k}}^0 s_z + 2\lambda \{ \cos(k_x d) - \cos(k_y d) \} s_x \quad (7)$$

where the Hamiltonian  $H_{\mathbf{k}}^0$  of spin-up component can be written as

$$\begin{aligned} H_{\mathbf{k}}^0 = & \delta \sigma_z \tau_z + \Omega \{ 1 - \cos(k_x d) \} \sigma_z \tau_x - \Omega \sin(k_x d) \sigma_z \tau_y \\ & - \Omega \sin(k_y d) \sigma_x - \Omega \{ 1 - \cos(k_y d) \} \sigma_y \\ & - t \sin(k_x d) \sin(k_y d) \sigma_x \tau_x \\ & - t \{ 1 + \cos(k_x d) + \cos(k_y d) + \cos(k_x d) \cos(k_y d) \} \sigma_y \tau_y \\ & + t \{ \sin(k_x d) + \sin(k_x d) \cos(k_y d) \} \sigma_y \tau_x \\ & + t \{ \sin(k_y d) + \sin(k_y d) \cos(k_x d) \} \sigma_x \tau_y \end{aligned} \quad (8)$$

Here  $d = 2a$  is the length of the enlarged unit cell.  $s_i$  is still Pauli matrices of hyperfine spin states ( $\uparrow, \downarrow$ ). Both  $\sigma_i$  and  $\tau_i$  correspond to Pauli matrices of orbit degree of freedom. Then the open boundary can be chosen along the edges of the folded BZ. The Hamiltonian (7) in the folded BZ respects reflection symmetries along the  $x$  and  $y$  directions with corresponding symmetry operators  $M_x = \sigma_z \tau_y s_x$  and

$M_y = \sigma_x s_x$  respectively, which anticommute with each other, i.e.  $\{M_x, M_y\} = 0$ . In general, the quantization of edge polarization and quadrupole moment are both protected by the reflection symmetries.

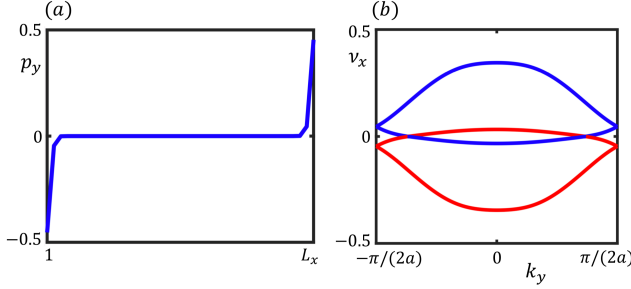


FIG. 3. (a) Edge polarization  $p_y$  with a lattice size along the  $x$  direction as  $L_x = 40$ . (b) Wannier bands for different values of  $k_y$ . Red and blue lines correspond to two different types of Wannier bands with eigenvalues  $\nu_x^+$  and  $\nu_x^-$  respectively. The parameters are chosen as  $\delta = 0.4t$ ,  $\omega = 0.8t$  and  $\lambda = 0.3t$ .

One can choose an open boundary along the  $x$  or  $y$  direction and estimate the edge polarization  $p_x^{\text{edge}}$  and  $p_y^{\text{edge}}$  respectively [1, 2]. As in Fig. 3(a), the edge polarization is quantized and non-zero when  $|\delta| < 4t$ , and a sudden change to zero can also be observed when  $|\delta| > 4t$ , which means that our system has an edge-corner correspondence.

The bulk topology is interesting in our system. The Wannier bands  $\nu_x$  as the set of Wannier centers along  $x$  as a function of  $k_y$  can be estimated by calculating the Wilson loop along the  $x$  direction in the folded BZ [1, 2]. As shown in Fig. 3(b), these Wannier bands are gapless, which is very different from the scenarios in Ref.[1, 2]. But because of the presence of the reflection symmetry, the distribution of these Wannier bands still satisfy the relation  $\nu_x^+ = -\nu_x^-$ . One can choose one Wannier sector, for example  $\nu_x^+$ , to estimate the quadrupole moment by calculating the nested Wilson loop, we just need to integrate along the Wannier sector  $\nu_x^+$ . We can calculate the non-Abelian nested Wilson loop of the two Wannier bands, instead of integrate them in turns. The result shows that the quadrupole moment is quantized and its value is  $1/2$  when  $|\delta| < 4t$ , which indicates that our system has a bulk-edge-corner correspondence. Our results also demonstrate that even when the Wannier bands is gapless, the quantized quadrupole moment can still be well-defined if the system has corresponding symmetries.

It's worth pointing out that the correspondence between the quantized edge polarization and zero corner modes is an intrinsic property of the system and it is irrelevant with the choice of the BZ. This can be verified by adding a very small perturbation to distinguish the amplitude of intra-cell and inter-cell NN tunneling  $\Omega$ , which would make the enlarged unit cell a primitive cell. We find that the topological properties is unchanged, which means that the above topological characterization is feasible and valid.

### III. TOPOLOGICAL PROPERTIES OF SYSTEM WITH NEAREST-NEIGHBOR ANISOTROPIC COUPLING

In the above discussion, we show that the emergence of topologically protected zero-energy corner states is intrinsically related to the NNNN anisotropic coupling. If the NNNN coupling is replaced by NN anisotropic coupling, SOTI will consequently be replaced by other interesting topological phenomena. In this section, we will discuss two different types of NN anisotropic coupling terms associated with two different lattice structures. Different types of lattice structure, which depend on the existence of dislocation between the two spin components as shown in Fig. 4, exhibit very different topological properties. In the first case, the corner states still exist but their energy is shift away from zero, and they are non-topologically protected states. In the second case, the system becomes a topological semimetal.

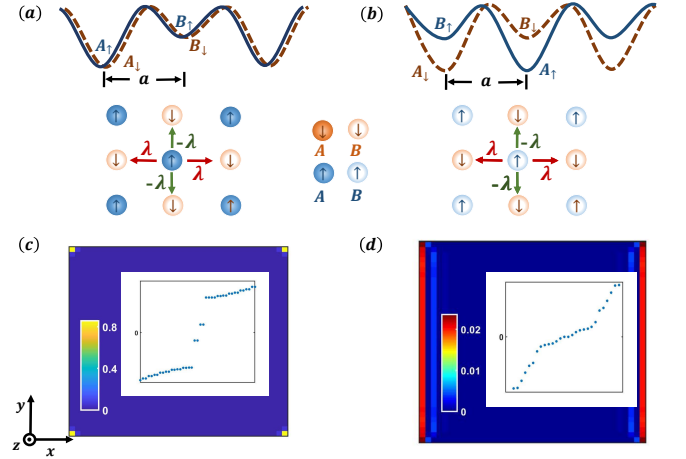


FIG. 4. The upper panels show the spin-independent lattice structures (a) for Hamiltonian (10) and (b) for Hamiltonian (13) as well as their corresponding NN coupling terms. The lower panels (c) and (d) depict the density distributions of nonzero-energy corner states in the system with Hamiltonians (10) and (13) respectively. The inset shows the energy spectrum of whole system. The parameters are set as  $\delta = -t$ ,  $\omega = t$ ,  $\lambda = 0.5t$  in panel (c) and  $\delta = 2t$ ,  $\omega = t$ ,  $\lambda = 0.5t$  in panel (d). The lattice size is fixed as  $L_x \times L_y = 40 \times 40$ .

#### A. Spin-independent lattice structure

We first consider the lattice structure without dislocation for different spin components, as shown in Fig. 4(a). The NN coupling term is expressed as

$$H_c = 2\lambda \{ \cos(k_x a) - \cos(k_y a) \} \sigma_x s_x \quad (9)$$

The tight-binding Hamiltonian in the momentum space is written as

$$H_{\mathbf{k}}^{(1)} = \{ \delta + 4t \cos(k_x a) \cos(k_y a) \} \sigma_z + 2\Omega \sin(k_x a) \sigma_y + 2\Omega \sin(k_y a) \sigma_x s_z + 2\lambda (\cos(k_x a) - \cos(k_y a)) \sigma_x s_x \quad (10)$$



By numerical calculations with open boundary along the  $x$  and  $y$  directions, we find that the energy of corner states shifts away from zero, see Fig. 5(a). Contrary to the result of the above section, the energy band has only one crossing point at  $\Gamma$  when  $\delta = -4t$  and the system is gapped in the whole BZ for other values of  $\delta$ , implying that the system is topologically trivial and the corner states are non-topologically protected.

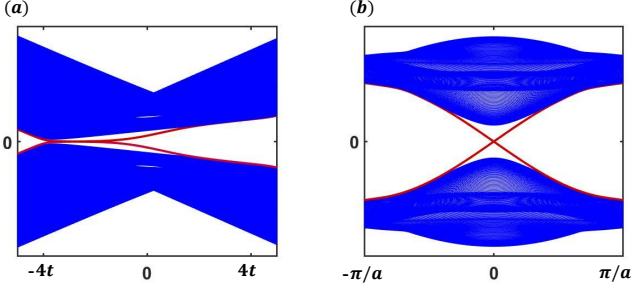


FIG. 5. (a) Energy spectrum of Hamiltonian (10) as the function of the effective energy detuning  $\delta$ . (b) Energy-band structure of Hamiltonian (13) with an open boundary along the  $y$  direction. The edge states are gapless with NN anisotropic coupling term of the second form. The parameters are chosen as  $\omega = t$ ,  $\lambda = t$  for panel (a) and  $\omega = t$ ,  $\lambda = 0.3t$  for panel (b).

The Hamiltonian (10) has a similar form with the Hamiltonian (1), except that the NNNN coupling term is replaced by the NN coupling. But in this case, the Hamiltonian in the folded BZ breaks the reflection symmetry, see the lattice structure in Fig. 5(a), which means that the edge polarization is not quantized. The topological properties of this system can also be explained by the effective edge theory. We expand the Hamiltonian around the point with a minimum band gap. According to the low-energy effective edge theory, we derive the effective Hamiltonian at the minimum-gap point  $\Gamma$  where  $\delta \rightarrow 4t$  that is the same as the low-energy Hamiltonian in Ref. [18], ensuring the existence of corner states. But when  $\delta \rightarrow -4t$ , the minimum of the gap is at  $M$  point and the Hamiltonian (10) expanded around  $M$  point reads

$$H_M^{(1)}(\mathbf{k}) = \{m' + 2ta^2(k_x^2 + k_y^2)\}\sigma_z - 2\Omega a(k_x\sigma_y - k_y\sigma_x s_z) - \lambda[4 - a^2(k_y^2 + k_x^2)]\sigma_x s_x \quad (11)$$

The effective coupling term is a constant with an amplitude of  $4\lambda$ , which indicates that the system is topologically trivial. One can find that the corner states are non-topologically protected in the parameter space of  $|\delta| < 4t$ , as shown in Fig. 5(a).

## B. Spin-dependent lattice structure

Next we consider the lattice structure with a dislocation between different spin components as shown in Fig. 4(b). In this case, the NN coupling term is

$$H_c = 2\lambda\{\cos(k_x a) - \cos(k_y a)\}s_x \quad (12)$$

The tight-binding Hamiltonian in the momentum space is

$$H_{\mathbf{k}}^{(2)} = \{\delta + 4t\cos(k_x a)\cos(k_y a)\}\sigma_z + 2\Omega\sin(k_x a)\sigma_y + 2\Omega\sin(k_y a)\sigma_x s_z + 2\lambda(\cos(k_x a) - \cos(k_y a))s_x \quad (13)$$

The anisotropic term breaks the combination  $\mathcal{IT}$  of the inversion symmetry and the time-reversal symmetry, resulting in a splitting of the two-fold degeneracy of energy bands, as depicted in Fig. 6. The Hamiltonian in the folded BZ still respects the reflection symmetry, but the corresponding symmetry operators along the  $x$  and  $y$  directions become the form of  $M_x = \sigma_z\tau_y s_y$  and  $M_y = \sigma_x s_x$  respectively. They commute with each other, which implies that there is no higher-order topological states in this case [1, 2]. By numerical calculations with a square geometry, we find that the topologically protected zero-energy corner states disappear, see Fig. 4(d). The band structure with an open boundary along the  $y$  direction is still gapless when  $\lambda \neq 0$ , see Fig. 5(b). This can also be derived from the effective edge theory. We can expand the Hamiltonian around  $\Gamma$  point when  $\delta \rightarrow -4t$

$$H_{\Gamma}^{(2)}(\mathbf{k}) = \{m - 2ta^2(k_x^2 + k_y^2)\}\sigma_z + 2\Omega a(k_x\sigma_y + k_y\sigma_x s_z) + \lambda a^2(k_y^2 - k_x^2)s_x \quad (14)$$

When considering the open boundary condition  $y > 0$ , this effective Hamiltonian is separated into two parts as  $H_{\Gamma}^{(2)}(k_x, -\partial_y) = H_0^{(2)} + H_p^{(2)}$  where  $H_0^{(2)}$  is same as in Eq. (3) and  $H_p^{(2)}$  can be written as

$$H_p^{(2)} = 2\Omega a k_x \sigma_y - \lambda a^2 \partial_y^2 s_x \quad (15)$$

We project  $H_p^{(2)}$  into the subspace consisting of the two zero-energy solutions of Eq.(5) and find

$$H_{y+}^{(2)}(k_x) \propto D_{y+} k_x s_z \quad (16)$$

We remark that the last term in  $H_p^{(2)}$  can not gap out the edge state, see Fig. 5(b). This result leads to the density distribution of wave functions as shown in Fig. 4(d) for a real space lattice.

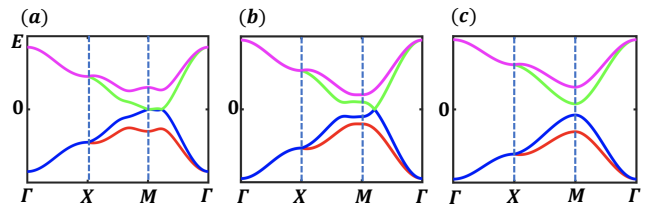


FIG. 6. Band structures of the Hamiltonian (13) for different values of  $\delta$ . (a) For  $\delta = 2.8t$ , the band structure has three band-crossing points. In particular, the band at the crossing point  $M$  has a quadratic dispersion. (b) For  $\delta = 3.6t$ , there is a pair of band crossing points with a linear dispersion along the  $k_y = 0$  line. (c) For  $\delta = 6.0t$ , it is a topologically trivial phase and no band touching point occurs. Here other parameters are set as  $\Omega = 0.8t$  and  $\lambda = 0.3t$ .

Although the Hamiltonian (13) do not support HOTI and corner states, it corresponds to a topological semimetal [38–40]. If the amplitude of  $\lambda$  is large enough, there exists one or two pairs of nodal points along the line  $k_y = 0$  when the values of  $\delta$  are in a certain range as shown in Fig. 6. On the  $k_y = 0$  line, the Hamiltonian (13) can be separated into two independent parts which include  $\sigma$  and  $s$  terms. The corresponding energy spectrum is

$$E(k_x) = \pm \sqrt{\{\delta + 4t \cos(k_x d)\}^2 + 4\Omega^2 \sin^2(k_x d)} \pm 2\lambda \{1 - \cos(k_x d)\}.$$

The solution to the equation  $E(k_x) = 0$ , if existing, will correspond to the position of nodal points. Two of the phase boundaries are estimated as  $\delta_c = 4(t \pm \lambda)$ , which implies that the band crossing point at  $M$  has a quadratic dispersion as  $\frac{\Omega^2}{2\lambda}(k_x^2 + k_y^2)$ . For  $\delta > 4(t + \lambda)$ , the system is topologically trivial and has no band touching points; while for  $\delta < 4(t + \lambda)$ , the crossing point of this band splits into two nodal points with a linear dispersion which move towards the opposite directions along the  $k_y = 0$  line, as shown in Fig. 6(c) and (b) respectively. At  $\delta = 4(t - \lambda)$ , another crossing point with a quadratic dispersion relation emerges at the  $M$  point, see Fig 6(a), which similarly splits into another pair of nodal points if  $\delta < 4(t - \lambda)$ . At another critical point, these two pairs of nodal points merge with each other and thus disappear, which further results in a topologically trivial system. We note that the value of  $\lambda$  at such a critical point depends on the values of other parameters in this system.

#### IV. CHIRAL HINGE MODES IN THREE-DIMENSIONAL SYSTEMS

Our system can be extended to 3D system by directly stacking 2D lattices along the  $z$  direction as shown in Fig. 7(a). By adding an additional NN tunneling and coupling along the  $z$  direction, one can construct a spin-dependent 3D checkerboard lattice with the Hamiltonian in the momentum space given by

$$\begin{aligned} H_{\mathbf{k}}^{3D} = & \{\delta + 4t \cos(k_x a) \cos(k_y a) + 2t_z \cos(k_z a)\} \sigma_z \\ & + 2\Omega \sin(k_x a) \sigma_y + 2\Omega \sin(k_y a) \sigma_x s_z \\ & + 2\lambda \{\cos(2k_x a) - \cos(2k_y a)\} \sigma_x s_x + 2\lambda_z \sin(k_z a) \sigma_x s_y \end{aligned} \quad (17)$$

When considering a periodic boundary condition along the  $z$  direction and open boundary with a square cross section in the  $x$ - $y$  plane, the change of chiral hinge modes can be observed in this system, which is related with a topological phase transition. As shown in Fig. 7, we just consider the case of  $t_z = t$  and  $\lambda_z = \lambda$  to simplify our discussion. As for  $|\delta| > 6t$ , the system is topologically trivial and no chiral hinge modes emerge. But when  $2t < |\delta| < 6t$ , there is one chiral mode along each hinge. When  $|\delta| < 2t$ , the corner states swing at each corner and have no chirality.

The topological properties of this system can be viewed as an effective 2D lattice system with an additional parameter  $k_z$ . In this case, the effective energy detuning of the 2D system is  $\delta_{3D} = \delta + 2t \cos(k_z a)$ , which is dependent on

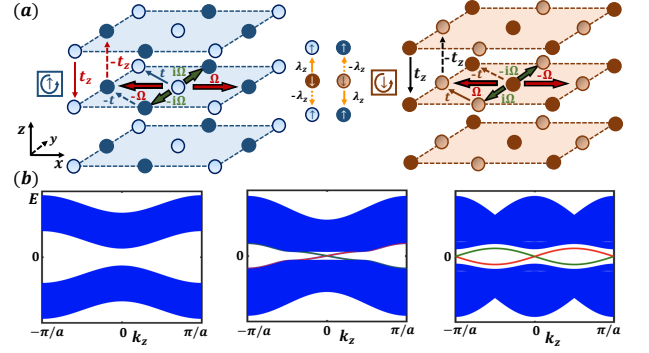


FIG. 7. (a) Scheme of the 3D SOTI. (b) Chiral hinge modes in the 3D system with open boundaries along the  $x$  and  $y$  directions. From the left to right panels, the energy detunings between  $A$  and  $B$  sublattices are  $\delta = -8t$ ,  $\delta = -4t$  and  $\delta = 0$  respectively, which correspond to zero, one and zero chiral hinge modes on each corner. Particularly, the corner states swing at each corner when  $\delta = 0$ .

$k_z$ . For  $|\delta| > 6t$ , the effective energy detuning  $|\delta_{3D}| > 4t$ , which implies that the system is topologically trivial. While for  $|\delta| < 2t$ , the effective energy detuning  $|\delta_{3D}| < 4t$ , indicating that the system is always topologically non-trivial. As compared with the original 2D Hamiltonian (1), the constant additional term  $2\lambda_z \sin(k_z a) \sigma_x s_y$ , which breaks the chiral symmetry, lifts zero energy of the corner states. When  $2t < |\delta| < 6t$ , the effective energy detuning  $\delta_{3D}$  varies from the topologically trivial to the non-trivial areas with the change of  $k_z$ , and the chiral hinge modes emerge.

#### V. THE SCHEME OF EXPERIMENTAL SETUP

Our scheme can be realized using periodically driven lattice. In our earlier work, we propose a scheme to realize an effective Hamiltonian [41]

$$\begin{aligned} H_{\mathbf{k},+} = & \{\delta + 4t \cos(k_x a) \cos(k_y a)\} \sigma_z \\ & + 2\Omega \sin(k_x a) \sigma_y + 2\Omega \sin(k_y a) \sigma_x \end{aligned} \quad (18)$$

which is the left-up block of Hamiltonian (1). We first load ultracold atoms in a 2D checkerboard superlattice with a lattice potential  $V(\mathbf{r}) = -V_0 \{\cos^2(k_0 x) + \cos^2(k_0 y) + 2 \cos \alpha \cos(k_0 x) \cos(k_0 y)\}$ , where  $V_0$  and  $\alpha$  are potential depth and the angle of polarization respectively, which can be well controlled in real experiments,  $k_0$  is the wave vector of the laser. The finite energy detuning prohibits the tunneling between NN sites. Then we adiabatically add a periodical circular driving on the checkerboard superlattice with the form  $x \rightarrow x + f \cos(\omega t)$ ,  $y \rightarrow y + f \sin(\omega t)$ , where  $f$  and  $\omega$  denote the driving amplitude and frequency respectively. In the Floquet framework, the effective Hamiltonian can be written as  $H - i\hbar \partial_t = [\mathbf{p} - \mathbf{A}(t)]^2 / (2m) + V(\mathbf{r}) - i\hbar \partial_t$ , where  $\mathbf{A}(t) = (fm\omega \sin(\omega t), fm\omega \cos(\omega t))$  can be considered as a temporally periodic synthetic gauge field which can induce an effective photon-assisted NN chiral tunneling.

To realize the Hamiltonian (1), we need to exploit two hyperfine spin states of ultracold atoms. Using two types of

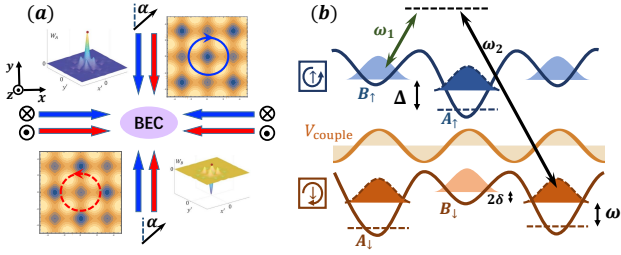


FIG. 8. Scheme of the experimental setup. (a) Realization of spin-dependent checkerboard lattices. Blue and red lines correspond to lasers trapping spin-up and spin-down components respectively. The polarizations of blue and red lasers along the  $x$  direction are parallel to the  $z$  direction but anti-parallel to each other, while the polarizations of lasers along the  $y$  direction are parallel to each other but have an angle  $\alpha$  with the  $z$  axis. The right upper and left lower insets are the lattice structures for spin-up and spin-down components. The clockwise and counter-clockwise circle correspond to the chirality of periodic driving. The left upper and right lower insets depict the Wannier functions of  $A$  and  $B$  sublattices respectively (b) The brown pattern is the form of coupling between different spin components. Red and purple wave packets correspond to the Wannier wave functions for the spin-up and spin-down components respectively. where  $x'$  and  $y'$  correspond to  $x + y$  and  $x - y$  directions. The red dots show the positions of  $(x, y) = (0, 0)$ , which means that the centers of two different types of Wannier functions have a displacement of  $a$ .

lasers with different frequencies, atoms of the different two hyperfine states can be trapped separately [43, 44]. By controlling the angle of polarization for different lasers, the spin-dependent checkerboard lattice can be realized, as shown in Fig. 8(a). We assume that the frequency difference of lasers does not induce visible difference of the wavelengths, and the lattice spacing for different spin components are approximately the same. Then by adiabatically adding periodically circular driving with opposite rotation directions for different hyperfine spin components, the effective Hamiltonian (1) with  $\lambda = 0$  can be simulated.

To simulate the off-diagonal terms which depend on  $\lambda$ , one can try to utilize an additional magnetic field along the  $z$  direction and a two-photon Raman process. Such a magnetic field induce an energy split  $\Gamma$  between different spin components. Two Raman lasers with the same wave vector  $k_0$  and an frequency difference  $\omega_2 - \omega_1 = \Gamma$  can be set as in Fig. 8(b), which implies that the Raman coupling is inhomogeneous with the form  $V_{\text{couple}}(x, y) = \Lambda \{ \cos(2k_0 y) - \cos(2k_0 x) \} |\uparrow\rangle\langle\downarrow|$ . [45, 46] The minus sign can be controlled by setting the relative phase between the two Raman lasers. Based on this setting, the on-site coupling will be cancelled because the Wannier function is symmetric along the  $x$  and  $y$  direction. The NN and NNN couplings along the  $x$  direction can be

estimated as

$$\begin{aligned} \lambda_{NN} &= \int W_A^*(x, y) V_{\text{couple}}(x, y) W_B(x, y) dx dy \\ \lambda_{NNN} &= \int W_A^*(x, y) V_{\text{couple}}(x, y) W_B(x + a, y + a) dx dy \\ \lambda_{NNNN} &= \int W_A^*(x, y) V_{\text{couple}}(x, y) W_A(x + 2a, y) dx dy \end{aligned} \quad (19)$$

where  $W_A(x, y)$  and  $W_B(x, y)$  are the Wannier functions of  $A$  and  $B$  sublattices of the original checkerboard lattices respectively, as shown in the inset of Fig. 8(a), the centers of two types of Wannier function have a displacement of  $a$ . We can verify that the amplitude of NNN coupling  $\lambda_{NNN}$  along the  $x \pm y$  direction can be ignored because of the orthogonality of Wannier functions. According to the form of Raman coupling, the NN and NNN couplings along the  $y$  direction have the same amplitude but opposite signs as compared to the ones along the  $x$  direction. From the form of Wannier functions, the amplitude of  $\lambda_{NN}$  always has the same order as  $\lambda_{NNNN}$ . To overcome the influence of  $\lambda_{NN}$ , we can engineer the form of Raman coupling more delicately. But actually we don't need to worry about the influence of  $\lambda_{NN}$ . From our discussion of the second case in section III, this type of NN coupling can not open the gap on the boundary, which means that it has no contribution to the higher-order topology. This result can also be verified by numerical calculation. Using the experimental feasible lattice potential  $V_0 = 2E_R$  ( $E_R = \hbar^2/(8ma^2)$  is the recoil energy),  $\alpha = 0.02$  and suitable Raman coupling strength, one can estimate that the amplitude of  $\lambda_{NNNN}$  is about  $0.01E_R$  when  $\Lambda$  is on the same order of  $E_R$ , which is on the order of  $nK$ . According to our calculation, the energy gap always depends on the amplitude of effective chiral tunneling induced by the lattice shaking when the amplitude of  $\lambda_{NNNN}$  is small. So we think all phenomena we discussed in our work can be observed in current experiments.

One can make use of several different methods to observe the topological properties in this system. The most direct method is to create a sharp open boundary on the  $x$  and  $y$  directions and measure the corner states directly by using the optical box as in Ref.[47] to create a sharp boundary. But in ultracold atom systems, we can also try to detect the topological properties of the bulk: (i) The first method is using the topological pumping. We can regard  $k_z$  in Hamiltonian (17) as a time-dependent parameter and try to change it adiabatically. Then the movement of particles towards two diagonal corners can be observed [48]; (ii) The second method is the direct measurement of the Wilson loop. By accelerating the optical lattice and with band mapping, one can realize the tomography of Berry curvature and Wilson loop [31, 32]. Then we can reconstruct the quantized quadrupole moment in the bulk.

## VI. CONCLUSION

As a conclusion, we investigate a second-order topological insulator with open boundary along special direction. With

the NNNN anisotropic coupling, zero-energy corner states emerge. We find that nested Wilson loop can also be well defined in the system with reflection symmetry even when the Wannier bands are gapless. We also extend our system to a 3D system and propose a 3D second-order topological insulator with chiral hinge modes. We hope our work will stimulate more explorations about the choice of open boundaries and the properties of higher-order topological quantum matters. In future, we will try to search for higher-order topological insulator systems which can be simulated more easily in real experiments. We will also extend our system into higher dimensions and explore more interesting quantum phenomena

because of the interplay between symmetries and high-order topological properties.

## ACKNOWLEDGEMENTS

We thank Xiang-Fa Zhou for his valuable suggestions. S. L. Zhang is supported by the Program of State Key Laboratory of Quantum Optics and Quantum Optics Devices (No:KF201903).

- 
- [1] W. A. Benalcazar, B. A. Bernevig, T. L. Hughes "Quantized electric multipole insulators", *Science* **357**, 61 (2017)
- [2] W. A. Benalcazar, B. A. Bernevig, and T. L. Hughes, "Electric multipole moments, topological multipole moment pumping, and chiral hinge states in crystalline insulators", *Phys. Rev. B*, **96**, 245115 (2017)
- [3] A. M. Cook, M. G. Vergniory, Z. Wang, S. S. P. Parkin, B. A. Bernevig, and T. Neupert, "Higher-order topological insulators", *Sci. Adv.* **eaat0346** (2018)
- [4] F. Zhang, C. L. Kane, and E. J. Mele, "Surface State Magnetization and Chiral Edge States on Topological Insulators", *Phys. Rev. Lett.* **110**, 046404 (2013)
- [5] Z. Song, Z. Fang, and C. Fang, "(d - 2)-Dimensional Edge States of rotation symmetry protected topological states", *Phys. Rev. Lett.* **119**, 246402 (2017)
- [6] J. Langbehn, Y. Peng, L. Trifunovic, F. Oppen, and P. W. Brouwer, "Reflection-symmetric second-order topological insulators and superconductors", *Phys. Rev. Lett.* **119**, 246401 (2017)
- [7] M. Ezawa "Higher-Order Topological Insulators and Semimetals on the Breathing Kagome and Pyrochlore Lattices", *Phys. Rev. Lett.* **120**, 026801 (2018)
- [8] C. H. Hsu, P. Stano, J. Klinovaja, and D. Loss, "Majorana Kramers Pairs in Higher-Order Topological Insulators", *Phys. Rev. Lett.* **121**, 196801 (2018)
- [9] X. Zhu, "Tunable Majorana corner states in a two-dimensional second-order topological superconductor induced by magnetic fields", *Phys. Rev. B*, **97**, 205134 (2018)
- [10] L. Trifunovic and P. W. Brouwer, "Higher-Order Bulk-Boundary Correspondence for Topological Crystalline Phases", *Phys. Rev. X*, **9**, 011012 (2019)
- [11] Y. Volpez, D. Loss, and J. Klinovaja, "Second-Order Topological Superconductivity in  $\pi$ -Junction Rashba Layers", *Phys. Rev. Lett.* **122**, 126402 (2019)
- [12] R. X. Zhang, F. Wu, and S. D. Sarma, "Möbius Insulator and Higher-Order Topology in  $\text{MnBi}_{2n}\text{Te}_{3n+1}$ ", *Phys. Rev. Lett.* **124**, 136407 (2020)
- [13] Y. Ren, Z. Qiao, and Q. Niu, "Engineering Corner States from Two-Dimensional Topological Insulators", *Phys. Rev. Lett.* **124**, 166804 (2020)
- [14] C. Chen, Z. Song, J. Z. Zhao, Z. Chen, Z. M. Yu, X. L. Sheng, and S. A. Yang, "Universal Approach to Magnetic Second-Order Topological Insulator", *Phys. Rev. Lett.* **125**, 056402 (2020)
- [15] M. Kheirkhah, Z. Yan, and F. Marsiglio, "Vortex-line topology in iron-based superconductors with and without second-order topology", *Phys. Rev. B*, **103**, 140502 (2021)
- [16] X. W. Luo, and C. Zhang, "Higher-Order Topological Corner States Induced by Gain and Loss", *Phys. Rev. Lett.* **123**, 073601 (2019)
- [17] W. P. Su, J. R. Schrieffer, and A. J. Heeger, "Solitons in Polyacetylene", *Phys. Rev. Lett.* **42**, 1698 (1979)
- [18] Z. Yan, F. Song, and Z. Wang, "Majorana Corner Modes in a High-Temperature Platform", *Phys. Rev. Lett.* **121**, 096803 (2018)
- [19] X. Zhu, "Second-Order Topological Superconductors with Mixed Pairing", *Phys. Rev. Lett.* **122**, 236401 (2019)
- [20] X. Zhu, "Tunable Majorana corner states in a two-dimensional second-order topological superconductor induced by magnetic fields", *Phys. Rev. B*, **97**, 205134 (2018)
- [21] R. X. Zhang, W. S. Cole, and S. D. Sarma, "Helical Hinge Majorana Modes in Iron-Based Superconductors", *Phys. Rev. Lett.* **122**, 187001 (2019)
- [22] X. Wu, W. A. Benalcazar, Y. Li, R. Thomale, C. X. Liu, and J. Hu, "Boundary-Obstructed Topological High- $T_c$  Superconductivity in Iron Pnictides", *Phys. Rev. X*, **10**, 041014 (2020)
- [23] L. Chen, B. Liu, G. Xu, and X. Liu, "Lattice distortion induced first- and second-order topological phase transition in a rectangular high- $T_c$  superconducting monolayer", *Phys. Rev. Research*, **3**, 023166 (2021)
- [24] X. H. Pan, K. J. Yang, L. Chen, G. Xu, C. X. Liu, and X. Liu, "Lattice-Symmetry-Assisted Second-Order Topological Superconductors and Majorana Patterns", *Phys. Rev. Lett.* **123**, 156801 (2019)
- [25] J. Alicea, "New directions in the pursuit of Majorana fermions in solid state systems", *Rep. Prog. Phys.* **75** 076501 (2012).
- [26] S. D. Sarma, M. Freedman and C. Nayak, "Majorana zero modes and topological quantum computation", *npj Quantum Inf* **1**, 15001 (2015)
- [27] F. Schindler, Z. Wang, M. G. Vergniory, A. M. Cook, A. Murani, S. Sengupta, A. Yu. Kasumov, R. Deblock, S. Jeon, I. Drozdov, H. Bouchiat, S. Guéron, A. Yazdani, B. A. Bernevig and T. Neupert, "Higher-order topology in bismuth", *Nat. Phys.* **14**, 918 (2018)
- [28] M. Serra-Garcia, V. Peri, R. Süsstrunk, O. R. Bilal, T. Larsen, L. G. Villanueva, and S. D. Huber "Observation of a phononic quadrupole topological insulator", *Nature* **555**, 342 (2018)
- [29] S. Imhof, C. Berger, F. Bayer, J. Brehm, L. Molenkamp, T. Kiessling, F. Schindler, C. H. Lee, M. Greiter, T. Neupert, and R. Thomale, "Topolectrical-circuit realization of topological corner modes", *Nat. Phys.* **14**, 925 (2018)



- [30] C. W. Peterson, W. A. Benalcazar, T. L. Hughes and G. Bahl, "A quantized microwave quadrupole insulator with topologically protected corner states", *Nature* **555**, 346(2018)
- [31] N. Fläschner, B. S. Rem, M. Tarnowski, D. Vogel, D.-S. Lühmann, K. Sengstock, and C. Weitenberg, "Experimental reconstruction of the Berry curvature in a Floquet Bloch band", *Science*, **352**, 1091 (2016)
- [32] T. Li, L. Duca, M. Reitter, F. Grusdt, E. Demler, M. Endres, M. Schleier-Smith, I. Bloch, and U. Schneider, "Bloch state tomography using Wilson lines", *Science* **352**, 1094 (2016)
- [33] G. Jotzu, M. Messer, R. Desbuquois, M. Lebrat, T. Uehlinger, D. Greif and T. Esslinger, "Experimental realization of the topological Haldane model with ultracold fermions". *Nature* **515**, 237–240 (2014).
- [34] K. Wintersperger, C. Braun, F. N. Ünal, A. Eckardt, M. D. Liberto, N. Goldman, I. Bloch and M. Aidelsburger, "Realization of an anomalous Floquet topological system with ultracold atoms". *Nat. Phys.* **16**, 1058–1063 (2020)
- [35] B. A. Bernevig and T. L. Hughes and S. C. Zhang "Quantum Spin Hall Effect and Topological Phase Transition in HgTe Quantum Wells", *Science* **314**, 1757 (2006)
- [36] X. Qian and J. Liu, L. Fu and J. Li "Quantum spin Hall effect in two-dimensional transition metal dichalcogenides", *Science* **346**, 1344 (2014)
- [37] S. Wu, V. Fatemi, Q. D. Gibson, K. Watanabe, T. Taniguchi, R. J. Cava and P. Jarillo-Herrero "Observation of the quantum spin Hall effect up to 100 kelvin in a monolayer crystal", *Science* **359**, 76 (2018)
- [38] A. A. Burkov and L. Balents, "Weyl Semimetal in a Topological Insulator Multilayer", *Phys. Rev. Lett.* **107**, 127205 (2011).
- [39] K. Sun, W. V. Liu, A. Hemmerich, and D. Sarma, "Topological semimetal in a fermionic optical lattice", *Nat. Phys.* **8**, 67 (2012).
- [40] J. M. Hou, "Hidden-Symmetry-Protected Topological Semimetals on a Square Lattice", *Phys. Rev. Lett.* **111**, 130403 (2013)
- [41] S. L. Zhang, L. J. Lang, and Q. Zhou, "Chiral d-Wave Superfluid in Periodically Driven Lattices", *Phys. Rev. Lett.* **115**, 225301(2015)
- [42] R. Jackiw, C. Rebbi, "Solitons with fermion number 1/2", *Phys-RevD*.**13**.3398(1976)
- [43] O. Mandel, M. Greiner, A. Widera, T. Rom, T. W. Hänsch, and I. Bloch, "Coherent Transport of Neutral Atoms in Spin-Dependent Optical Lattice Potentials", *Phys. Rev. Lett.* **91**, 010407 (2003)
- [44] P. Soltan-Panahi, J. Struck, P. Hauke, A. Bick, W. Plenkers, G. Meineke, C. Becker, P. Windpassinger, M. Lewenstein, and K. Sengstock, "Multi-component quantum gases in spin-dependent hexagonal lattices", *Nat. Phys.* **7**, 434 (2011).
- [45] Z. Wu, L. Zhang, W. Sun, X.-T. Xu, B.-Z. Wang, S.-C. Ji, Y. Deng, S. Chen, X.-J. Liu, and J.-W. Pan, "Realization of two-dimensional spin-orbit coupling for Bose-Einstein condensates", *Science*, **354**, 86 (2016)
- [46] Z. Y. Wang, X. C. Cheng, B. Z. Wang, J. Y. Zhang, Y. H. Lu, C. R. Yi, S. Niu, Y. J. Deng, X. J. Liu, S. Chen, and J. W. Pan, "Realization of an ideal Weyl semimetal band in a quantum gas with 3D spin-orbit coupling", *Science* **372**, 271 (2021).
- [47] A. L. Gaunt, T. F. Schmidutz, I. Gotlibovych, R. P. Smith, and Z. Hadzibabic, "Bose-Einstein Condensation of Atoms in a Uniform Potential", *Phys. Rev. Lett.* **110**, 200406 (2013)
- [48] J. F. Wienand, F. Horn, M. Aidelsburger, J. Bibo, and F. Grusdt, "Thouless Pumps and Bulk-Boundary Correspondence in Higher-Order Symmetry-Protected Topological Phases", [arXiv:2111.02491](https://arxiv.org/abs/2111.02491)